Enhanced electrocatalytic activity of a layered triple hydroxide (LTH) by modulating the electronic structure and active sites for efficient and stable urea electrolysis

Sustainable Energy & Fuels

ROYAL SOCIETY OF CHEMISTRY

PAPER

Enhanced electrocatalytic activity of a layered triple hydroxide (LTH) by modulating the electronic structure and active sites for efficient and stable urea electrolysis†

Cite this: DOI: 10.1039/d1se01478a

Komal Patil,[a] Pravin Babar,[b] Hyojung Bae,[c] Eunae Jo,[a] Jun Sung Jang,[a] Pravin Bhoite,[d] Sanjay Kolekar[e] and Jin Hyeok Kim*[a]

Received 19th September 2021
Accepted 24th November 2021

DOI: 10.1039/d1se01478a

rsc.li/sustainable-energy

A clean and sustainable "hydrogen-based economy" will usher in a new era. Therefore, the hydrogen production pathway is crucial. Diligent urea ($CO(NH_2)_2$) electrolysis has recently been investigated as a promising energy-saving approach for renewable hydrogen production compared to conventional water (H_2O) electrolysis. This is because of the minimal cell voltage, mitigation of urea-rich wastewater, and availability of electrocatalysts. Herein, we report trimetallic nickel–cobalt–iron layered triple hydroxide nanosheets (NiCoFe-LTH) grown on nickel foam (NF) *via* a one-step hydrothermal synthesis method. They were tested as catalysts for the urea oxidation reaction (UOR) and hydrogen evolution reaction (HER) in direct urea fuel cells (DUFCs). NiCoFe-LTH/NF behaves as a highly active durable 2D catalyst electrode for the UOR and HER with the required potentials of 1.337 V and 180 mV to achieve catalytic current densities of 25 and 10 mA cm^{-2} respectively, in 1 M KOH with 0.33 M urea. Moreover, this electrode also performs well in urea-electrolysis, requiring a very small potential of 1.49 V to achieve 10 mA cm^{-2} over a period of 30 h. The developed urea electrolyzer is very effective at producing H_2. It is cost-effective and involves no difficulties in material synthesis or electrolyzer fabrication, paving the way for the development of clean renewable energy infrastructure.

1. Introduction

Growing awareness about global warming and fossil fuel depletion has made the development of renewable energy production and storage technologies an important albeit challenging task.[1–3] Direct urea fuel cells (DUFCs) have recently been approved as potential clean energy devices, utilizing urea/urine-containing wastewater as fuel and low-cost catalyst materials (Scheme 1).[4–6] DUFCs are based on the reaction $2CO(NH_2)_2 + 3O_2 \rightarrow 2N_2 + 4H_2O + 2CO_2$. The reaction produces power while simultaneously treating urea-rich wastewater before it naturally hydrolyzes in the ecosystem.[7–10] When urea electrolysis is used instead of conventional water splitting, the thermodynamic potential can be reduced from 1.23 V to 0.37 V.[11–13] The anodic UOR, $(CO(NH_2)_2 + 6OH^- \rightarrow N_2 + 5H_2O + CO_2 + 6e^-)$ has slower kinetics than the cathodic HER due to a $6e^-$ transfer process and requires the use of electrocatalysts to speed up the reaction rate.[14–19] High performance UOR catalysts are required to reduce the overpotential and drive the sluggish reaction.[20–22] Usually, noble-metal-based catalysts, such as Rh/Pd and Pt/C, are required to catalyze the UOR to ensure a faster reaction rate.[23–25] However, the use of expensive catalysts restricts the commercialization and large-scale application of the UOR

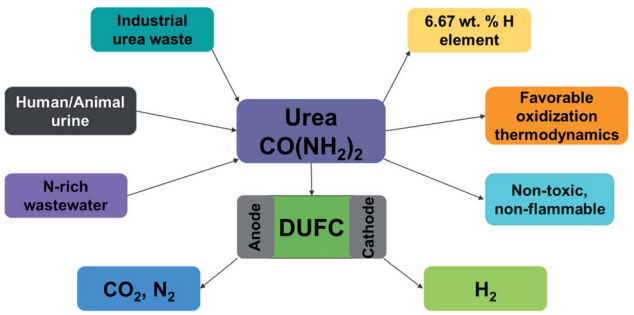

Scheme 1 An illustration of the direct urea-to-hydrogen process.

[a]Optoelectronic Convergence Research Center, Department of Materials Science and Engineering, Chonnam National University, Gwangju 500-757, South Korea. E-mail: jinhyeok@chonnam.ac.kr
[b]KAUST Catalysis Center, Physical Sciences and Engineering (PSE), King Abdullah University of Science and Technology (KAUST), Thuwal 23955, Saudi Arabia
[c]Optoelectronic Convergence Research Center, Chonnam National University, Gwangju 61186, South Korea
[d]Department of Chemistry, Kisan Veer Mahavidyalaya, Wai, Maharashtra, 412803, India
[e]Department of Chemistry, Shivaji University, Kolhapur 416004, Maharashtra, India

† Electronic supplementary information (ESI) available. See DOI: 10.1039/d1se01478a

technique.[7,26,27] Furthermore, developing a high-performance anodic UOR catalyst and a cathodic HER catalyst from the same low-cost precursor materials will streamline the process and minimize production costs.[28,29] Much research has been devoted to the development of efficient electrocatalysts from earth-abundant materials, including transition-metal oxides, (oxy)hydroxides, sulfides, nitrides, carbides, metal–organic frameworks (MOFs), and covalent organic frameworks (COFs), among others, to replace noble-metal-based catalysts.[30–35] Among them, NiCo layered double hydroxide (NiCo-LDH) possesses many favorable attributes for use as an efficient electrocatalyst for urea electrolysis, including two-dimensional (2D) nanosheet morphology, tunable electronic structure, and good stability.[20,25,36–39] However, major drawbacks, such as the limited active sites and low conductivity, imply that NiCo-LDH does not fulfill all the requirements of an electrocatalyst. Different strategies have been employed to improve the catalytic activities of catalysts. These include increasing the number of active sites by surface incorporation, fabricating unique nanostructures, and enhancing the intrinsic properties of catalysts by modulating the electronic structure.[40–42] The addition or incorporation of metal elements has been effective in altering the catalytic properties and electronic structure at the atomic level.[43,44] The alteration of the electronic structure can generate a valence change of the elements. It also helps to promote water dissociation and adsorption capacity of different reaction intermediates, which, in turn, helps to improve the electrocatalytic performance.[45] In particular, Fe when combined with Co^{2+} or Ni^{2+} has recently been shown to significantly affect the coordination structure by partial charge transfer and to reallocate electronic density.[37,46–49] Therefore, the synergy between metals with different valence electronic configurations can easily modify the local coordination and electronic structure of the catalyst, thus enhancing the electrocatalytic activity.[45] Therefore, it can be expected that the incorporation of Fe into nickel–cobalt-based (oxy)hydroxides will intrinsically facilitate the OER activity and, therefore UOR activity.

Encouraged by the above-mentioned factors, we present our recent work. Trimetallic nickel–cobalt–iron layered triple hydroxide (NiCoFe-LTH) nanosheets grown on NF by a one-step hydrothermal synthesis could act as a versatile and high-performance electrode for catalyzing both overall water-splitting and urea-electrolysis simultaneously. These nanosheets show good overall water-splitting efficiency requiring a cell voltage of 1.65 V to achieve 10 mA cm^{-2}. This material also has excellent catalytic activity, selectivity, and durability for the UOR with an ultralow potential of 1.337 V *vs.* RHE at an anodic current density of 25 mA cm^{-2}, as added benefits, outperforming all previously reported transition-metal-based UOR catalysts (Table S1†). A urea-assisted energy-saving alkaline hydrogen production system was also built here by substituting the anodic oxygen evolution reaction (OER) with UOR, with the goal of improving the overall water-electrolysis efficiency. This urea-electrolysis configuration actuated by NiCoFe-LTH/NF provides 10 mA cm^{-2} at a low voltage of 1.49 V, which is 160 mV lower than the urea-free counterpart and comparable to other reported catalyst performances (Table S3†). The catalytic performance of NiCoFe-LTH/NF could be attributed to the high intrinsic activity, large surface area, and metallic features of the NiCoFe-LTH phase. The nanosheet configuration exposes more catalytically active sites and accelerates the diffusion of the electrolyte and the generated gas bubbles. In addition, the triple hydroxide structure and mixed-valence states of Ni, Co, and Fe in the NiCoFe-LTH phase offer a variety of redox reactions.

2. Experimental section

2.1 Reagents

High purity (>99%) nickel(II) nitrate hexahydrate ($Ni(NO_3)_2 \cdot 6H_2O$), cobalt(II) nitrate hexahydrate ($Co(NO_3)_2 \cdot 6H_2O$), iron(III) nitrate nonahydrate ($Fe(NO_3)_3 \cdot 9H_2O$), urea (CH_4N_2O), and cetyltrimethylammonium bromide (CTAB) were purchased from Sigma-Aldrich and used as received. The NF substrate (thickness, 1.6 mm; surface density, 420 g cm^{-2}) was purchased from Alantum Korea. Ultrapure deionized water was obtained from a Millipore system.

2.2 Synthesis of NiCoFe-LTH and NiCo-LDH on NF

A simple hydrothermal method was used to grow NiCoFe-LTH nanosheets on NF. Prior to use, NF (1 cm × 1 cm) was immersed in a 3 M hydrochloric acid solution and then ultrasonicated in acetone, ethanol, and DI water for 5 min each. Thereafter it was dried at 45 °C in a hot air oven. $Ni(NO_3)_2 \cdot 6H_2O$ (0.262 g), 0.175 g of $Co(NO_3)_2 \cdot 6H_2O$, 0.0175 g of $Fe(NO_3)_3 \cdot 9H_2O$, and 0.5 g of CTAB were dissolved in 30 mL of anhydrous methanol and 6 mL of DI water. The solution was magnetically stirred for 15 min to form a homogeneous solution, which was then transferred to a 50 mL Teflon-lined autoclave vessel. The pre-cleaned NF was then immersed in the precursor solution. Subsequently, the autoclave was heated at 180 °C for 24 h, and the reaction system was allowed to cool naturally. The NF was separated from the reaction mixture, cleaned with ethanol and water several times, and dried at 45 °C overnight to obtain NiCoFe-LTH nanosheets. NiCo-LDH nanosheets were also synthesized for comparison under the same conditions, with the exception of the iron source. The mass loading of the catalysts was calculated by weighing the NF before and after catalyst deposition. The total mass loading of NiCoFe-LTH/NF was 0.0181 g.

2.3 Physical characterizations

X-ray diffraction (XRD) patterns were evaluated over the 5–90° range on a PANalytical Empyrean 2θ diffractometer (PANalytical B.V., Netherlands) using a Cu X-ray source (Kα, 1.54 Å). The surface morphology was characterized using field-emission scanning electron microscopy (FE-SEM, JSM-6701F, JEOL, Japan) equipped with an energy dispersive X-ray (EDX) analyzer. Transmission electron microscopy (TEM) and high-resolution transmission electron microscopy (HRTEM) were performed on an FEI Tecnai G2 F30 (FEI, Netherlands) instrument equipped with an X-ray energy dispersive spectrometer at an operating voltage of 200 kV. X-ray photoelectron spectroscopy (XPS) profiles were recorded on an ESCALAB-MKII 250 photoelectron spectrometer (VG Co. UK) with Al Kα radiation.

2.4 Electrochemical measurements

All electrochemical measurements were performed on a WonATech, WMPG1000 Multichannel Potentiostat/Galvanostat (ver. 1.11) using a three-electrode system at room temperature (25 °C). The catalysts were measured in a 1 M KOH aqueous solution using a typical three-electrode configuration, in which either NiCoFe-LTH or NiCo-LDH was used as the working electrode, and Pt wire and the Ag/AgCl electrode were used as the counter and reference electrodes, respectively. Linear sweep voltammetry (LSV) was conducted in an O_2-saturated 1 M KOH electrolyte at a scan rate of 1 mV s^{-1}. Stability tests were performed at a constant current density of 25 mA cm^{-1}. The electrochemically active surface areas (ECSAs) were determined based on the double-layer capacitance (C_{dl}) using cyclic voltammetry (CV). The cyclic voltammograms were recorded in a non-faradaic potential range of 0.30–0.42 V *vs.* Ag/AgCl. All potentials were converted to the reversible hydrogen electrode (RHE) using the following formula:[50,51] $E_{RHE} = E_{Ag/AgCl} + 0.197 + 0.059 \times pH$. Electrochemical impedance spectroscopy (EIS) data were measured in the frequency range of 0.1–100 kHz at an AC amplitude of 10 mV. Turnover frequency (TOF) values were calculated at potentials of 1.4 V–1.7 V with respect to RHE with a regular interval of 0.05 V. The following equation was used in the calculation of the TOF for urea electrolysis:[52]

$$\mathrm{TOF} = \frac{j \times N_A}{n \times F \times \tau} \quad (1)$$

where j is the current density at a given potential, N_A is Avogadro's number (6.022×10^{23} mol^{-1}), n is the number of electrons transferred for the complete oxidation of urea ($n = 6$, in this case), F is the Faraday constant (96 485.3 C mol^{-1}), and τ denotes the number of electrochemically accessible active sites of NiCoFe-LTH/NF. Mass activity was calculated using the equation – j/m, where j is the current density (A m^{-2}) at a particular potential, and m is the catalyst loading mass. The specific activity was calculated using the equation, – j/A where j is the current density and A is the Brunauer–Emmett–Teller (BET) surface area of the catalyst. The performance measurement of urea electrolysis was characterized by the polarization curves in a two-electrode configuration in 1 M KOH with 0.33 M urea at a scan rate of 5 mV s^{-1}. Stability tests were performed using a constant current density of 10 mA cm^{-1}. All polarization curves in this study are mentioned without *iR*-correction.

3. Results and discussion

3.1 Morphological and structural characterizations of NiCoFe-LTH/NF

The synthesis procedure for the NiCoFe-LTH/NF nanosheets includes a one-step hydrothermal process, as illustrated in Fig. 1a. The phase purity and crystallographic structures of NiCo-LDH and NiCoFe-LTH were determined using XRD analysis. The XRD pattern of the as-prepared NiCo-LDH nanosheets is consistent with the previously reported NiCo-LDH structure and is in good agreement with the well-known hydrotalcite-like phase (JCPDS No. 38-0715).[53] As shown in Fig. 1b, the strong diffraction peaks at 44.6°, 51.8°, and 76.4° correspond to the (111), (200), and (220) planes of NF, respectively.[54] Additionally, the characteristic diffraction peaks at 11.08°, 22.15°, 34.41°, 38.63°, 45.16°, 60.15°, and 61.25° can be ascribed to the (003),

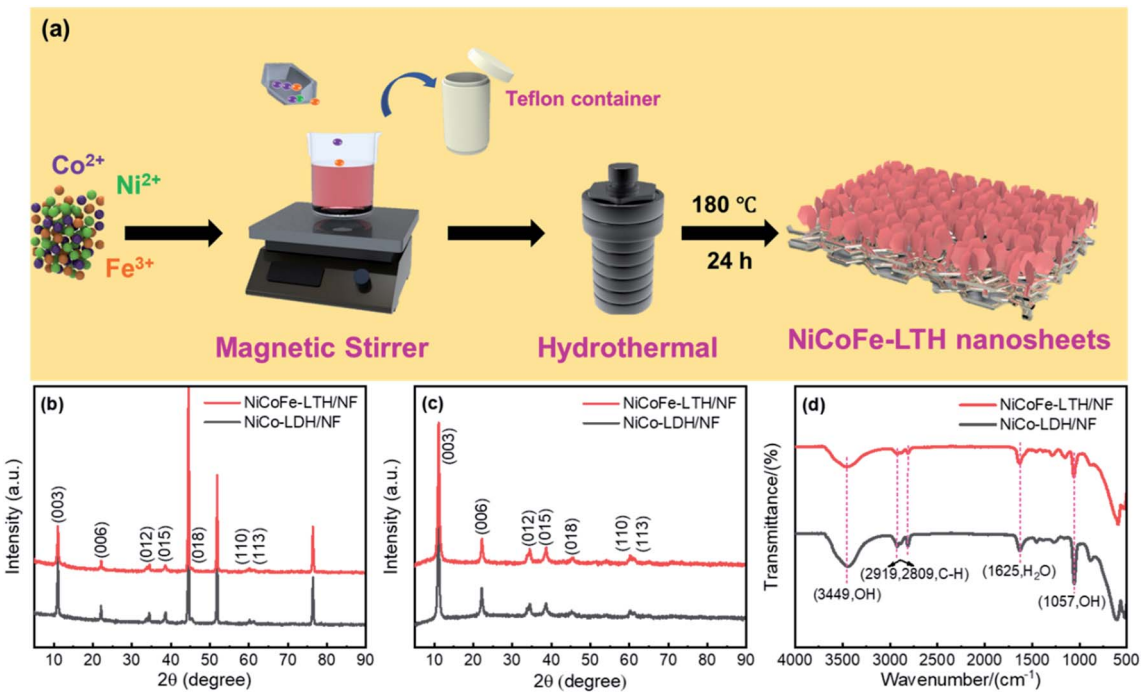

Fig. 1 (a) Schematic of the synthesis and structure of the NiCoFe-LTH nanosheets on NF, (b) XRD patterns of NiCoFe-LTH/NF and NiCo-LDH/NF, (c) powder XRD patterns of NiCoFe-LTH and NiCo-LDH, (d) FTIR spectra of NiCoFe-LTH and NiCo-LDH.

(006), (012), (015), (018), (110), and (113) crystalline planes of NiCo-LDH, respectively. No additional diffraction peaks were observed with Fe addition in NiCo-LDH. However, the intensity of the main diffraction peaks of NiCoFe-LTH decreased.[51,55] Fig. 1c displays the XRD pattern of the powder sample of NiCoFe-LTH, which also shows the same diffraction peaks as shown in Fig. 1b. Fourier transform infra-red spectroscopy (FTIR) was used to monitor the changes in NiCo-LDH following the hydrothermal reaction with the addition of the Fe precursor. A strong and broad absorption peak at 3449 cm^{-1} and another peak at 1057 cm^{-1} can be attributed to the stretching vibration of the O–H group (Fig. 1d).[56] The broad nature of the OH band is attributed to the existence of hydrogen bonding between the layered hydroxides, interlayer water, and anions in the interlayer gap. The IR bands in the region of 2800–2950 cm^{-1} were assigned to the C–H stretching vibration originating from the $-CH_3$ group in methanol. The band at 1625 cm^{-1} corresponds to H–OH vibration. The bands between 525 and 640 cm^{-1} are attributed to the metal–oxygen vibrations in the layers, which are typical of layered materials such as LDHs.[55,57,58]

XPS was employed to investigate the elemental compositions and valence states of the samples. The XPS survey spectrum of NiCoFe-LTH/NF confirmed the presence of all the elements Ni, Co, Fe and O (Fig. S1a†). Fig. 2a displays the Ni 2p orbital spectra of NiCo-LDH and NiCoFe-LTH. The characteristic peaks at 855.59 and 873.33 eV are assigned to the Ni $2p_{3/2}$ and Ni $2p_{1/2}$ orbitals of NiCo-LDH, respectively. They show a negative shift of approximately 0.10 to 0.20 eV for the NiCoFe-LTH catalyst.[59] In Fig. 2b, the peaks at the binding energies of 781.47 and 796.84 eV correspond to the Co $2p_{3/2}$ and Co $2p_{1/2}$ of Co^{2+}, respectively. The peaks fitting at 779.9 and 796.2 eV are associated with Co^{3+}.[60] Co, similar to Ni, shows a shift towards a lower binding energy in the NiCoFe-LTH sample, which could be attributed to the partial transfer of electrons from Fe to Ni/Co after Fe incorporation.[49,61,62] The high-resolution XPS profiles of the Fe 2p orbital for NiCoFe-LTH (Fig. 2d) show three characteristic peaks. The peaks at the binding energies of 714.5 and 725.1 eV, are indexed to the Fe^{3+} $2p_{3/2}$ and $2p_{1/2}$ orbitals, respectively. The peak at 717.6 eV corresponds to a satellite peak.[63,64] The high-resolution O 1s orbital spectrum of NiCo-LDH and NiCoFe-LTH is shown in Fig. 2c. It is deconvoluted into three peaks, O1, O2, and O3, related to metal–oxygen bonding, surface hydroxyl groups, and physisorbed and chemisorbed water, respectively.[49,60,65] All the O 1s orbital peaks in the NiCoFe-LTH/NF sample also show a slight shift to a lower binding energy as compared to that in the NiCo-LDH/NF sample, implying strong electronic interactions between the hydroxide layers.[49] It was demonstrated from the XPS results that Fe was successfully incorporated into NiCo-LDH. N_2 adsorption–desorption isotherms were obtained to characterize the surface area and pore size distributions of NiCoFe-LTH/NF (Fig. 2e) and NiCo-LDH/NF (Fig. S1b†). NiCoFe-LTH/NF possessed a higher specific surface area of 37.143 $m^2\ g^{-1}$ than that of NiCo-LDH/NF (32.5 $m^2\ g^{-1}$), which indicates that Fe incorporation provides more active sites for the urea-electrolysis process (Fig. 2e). In addition, the pore size distribution was in the range of 10–50 nm (inset of Fig. 2e), which facilitated the transfer of electrons and active intermediates.[66]

FE-SEM and TEM were used to study the morphological characteristics of all films after the hydrothermal reaction. SEM images of blank NF show a smooth surface as displayed in Fig. S2.† SEM images of NiCo-LDH (Fig. 3a) show densely dispersed nanosheets on the surface of the NF substrate. The vertical orientation of the nanosheets offers a large number of active sites and open areas for rapid ion transport.[23] However, NiCoFe-LTH (Fig. 3e) did not show any change in morphology compared to NiCo-LDH, indicating that NiCoFe-LTH retained its nanosheet structure. The morphology and 2D microstructure of the NiCoFe-LTH catalyst were further studied by TEM and HRTEM to confirm the formation of nanosheets. Fig. 3b and f further confirm the nanosheet structures of NiCo-LDH and NiCoFe-LTH, respectively. Selected area electron diffraction (SAED) patterns in the insets of Fig. 3b and f clearly show the diffraction rings, further confirming the crystallinity of both

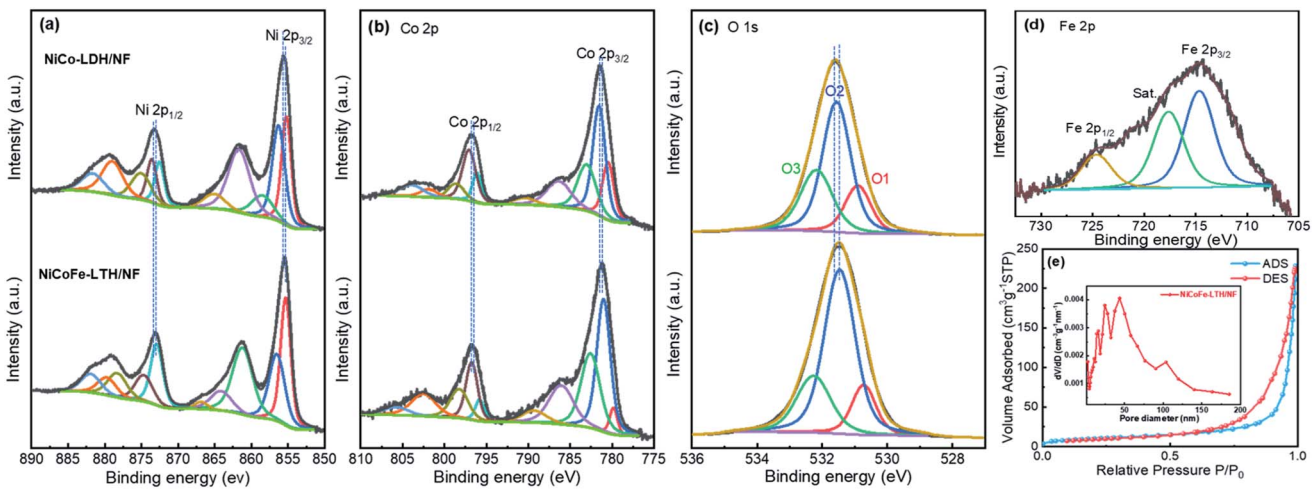

Fig. 2 High-resolution XPS profiles of (a) Ni 2p, (b) Co 2p, (c) O 1s, and (d) Fe 2p of NiCo-LDH/NF and NiCoFe-LTH/NF; (e) N_2 adsorption and desorption isotherms and pore size distribution of NiCoFe-LTH/NF.

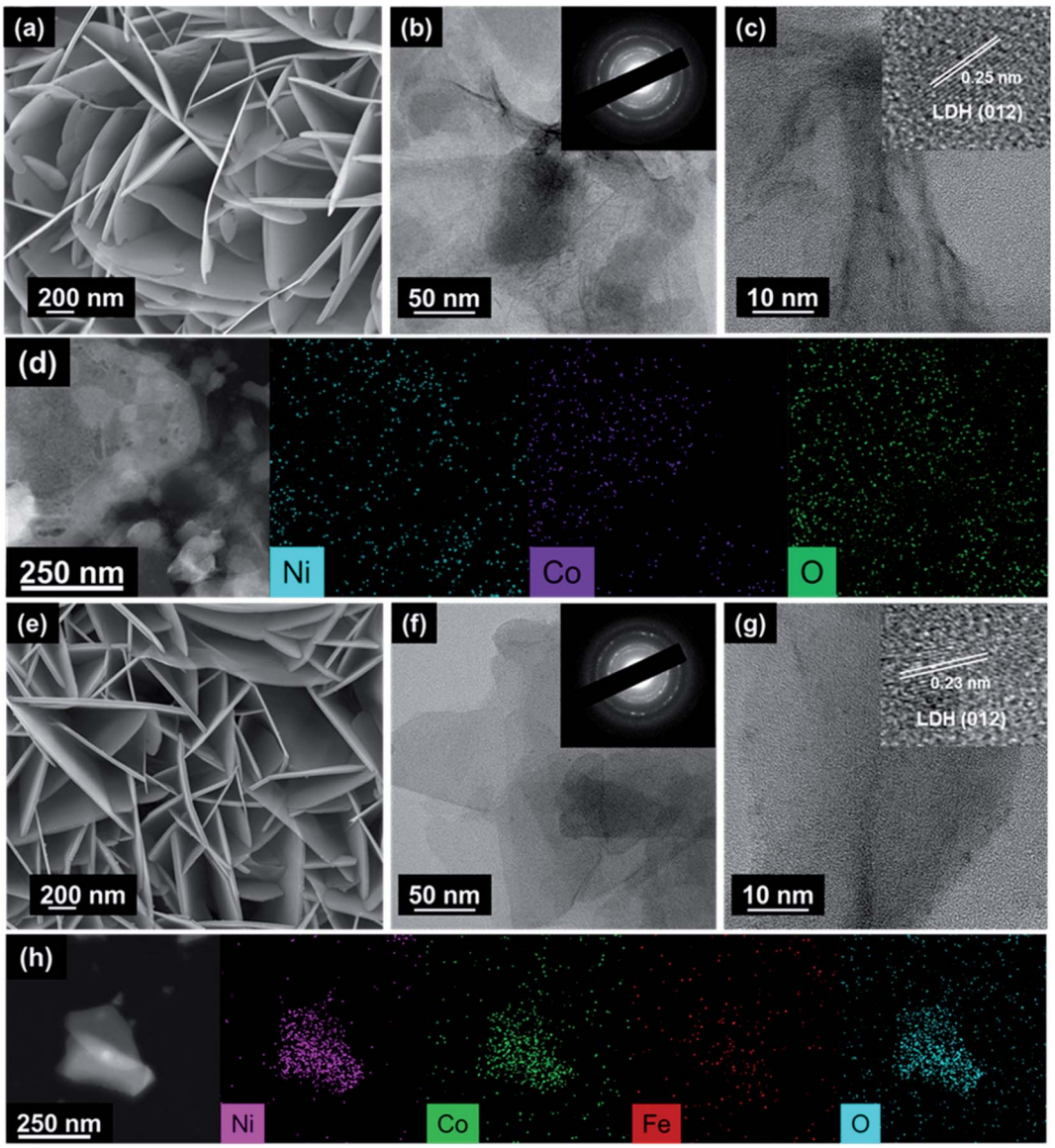

Fig. 3 (a–d) SEM, TEM, HRTEM, and STEM-EDX mapping images of NiCo-LDH/NF, (e–h) SEM, TEM, HRTEM, and STEM-EDX mapping images of NiCoFe-LTH/NF. The insets in (b and f) show the corresponding SAED patterns.

samples. In the HRTEM images (Fig. 3c and g), a distinguishable lattice fringe was observed. It was indexed to the (012) plane, with an interlayer spacing of 0.25 nm and 0.23 nm for NiCo-LDH/NF and NiCoFe-LTH/NF, respectively. Fig. 3d and h show the STEM-EDX mapping images of NiCo-LDH and NiCoFe-LTH, respectively, and illustrate the existence and uniform distribution of Ni, Co, Fe, and O elements.

3.2 Electrocatalytic performances for the UOR and HER

We then examined the OER and UOR activities of the as-prepared NiCo-LDH/NF and NiCoFe-LTH/NF materials using a three-electrode configuration in 1 M KOH with and without 0.33 M urea. Polarization curves for the UOR (with their OER activities for comparison) of the NiCoFe-LTH, NiCo-LDH, and RuO_2 catalysts are shown in Fig. 4a. As observed, the OER occurs on NiCo-LDH and RuO_2 in 1.0 M KOH at 25 mA cm^{-2} at a potential of 1.538 V and 1.55 V, respectively, whereas in the case of the UOR, a potential of 1.379 and 1.35 V is required respectively. The oxidation peak at approximately 1.348 V could be ascribed to the transformation of Ni(II) into Ni(III), which has been commonly observed in the literature.[67] In contrast, NiCoFe-LTH/NF yields a much greater UOR catalytic activity with a lower potential of 1.337 V to achieve 25 mA cm^{-2} in 1 M KOH with 0.33 M urea. However, the OER requires a much larger potential of 1.482 V to achieve the same current density of 25 mA cm^{-2}. It can be observed that a lower potential is required for NiCo-LDH/NF and NiCoFe-LTH/NF to reach the same current density in 1 M KOH with 0.33 M urea. Fig. 4b shows the UOR performances of all the catalysts. NiCoFe-LTH requires less potential (1.337 V) than NiCo-LDH (1.379 V), RuO_2 (1.35 V), and bare NF (1.475 V) to yield a current density of 25 mA cm^{-2}

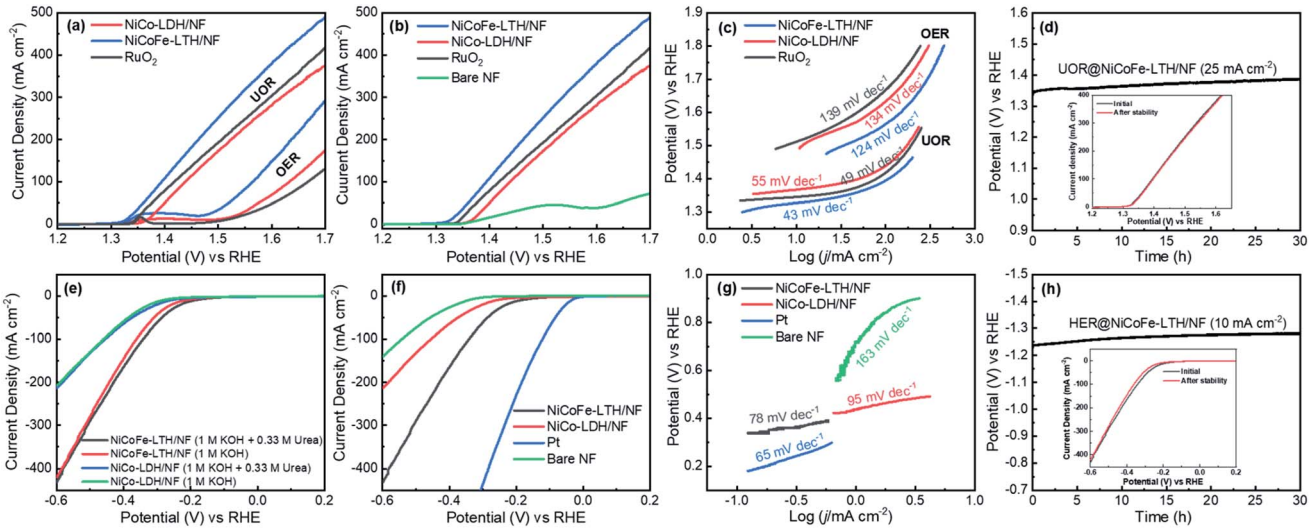

Fig. 4 Electrocatalytic UOR and HER performances. (a) Polarization curves for the UOR and OER of NiCo-LDH/NF, NiCoFe-LTH/NF, and RuO_2. (b) Comparison of the UOR activities of various catalysts, (c) Tafel plots for the UOR and OER derived from figure (a), (d) long-term stability test over 30 h of NiCoFe-LTH/NF for the UOR (polarization curves before and after the stability test in the inset), (e) polarization curves of NiCo-LDH/NF, NiCoFe-LTH/NF, and Pt for the HER in 1 M KOH with and without 0.33 M urea, (f) comparison of the HER activities of various catalysts, (g) Tafel plots for the HER derived from figure (f), (h) long-term stability test over 30 h of NiCoFe-LTH/NF for the HER (inset: polarization curves before and after the stability test).

(Fig. 4b). The corresponding Tafel slopes of all the catalysts were used to investigate the UOR kinetics. The NiCoFe-LTH/NF, RuO_2, and NiCo-LDH catalysts have very small Tafel slopes of 43, 49 and 55 mV dec^{-1}, respectively, for the UOR process (Fig. 4c). These values are substantially lower than those of NiCoFe-LTH/NF (124 mV dec^{-1}), RuO_2 (139 mV dec^{-1}), and NiCo-LDH/NF (136 mV dec^{-1}) indicating fast UOR reaction kinetics. Moreover, the long-term stability of NiCoFe-LTH during the UOR was studied by chronopotentiometric measurements at 25 mA cm^{-2} for 30 h. Fig. 4d indicates that NiCoFe-LTH was stable over this period. The LSV curve (as observed by chronopotentiometry) of NiCoFe-LTH/NF after the stability test is similar to that prior to the stability test, albeit with a negligible loss after 30 h (inset of Fig. 4d).

Fig. 4e shows the LSV curves of NiCoFe-LTH/NF and NiCo-LDH/NF in 1 M KOH with and without 0.33 M urea, suggesting that the presence of urea does not cause a significant decrease in HER activity. As expected, Pt has shown excellent HER activity (Fig. 4f). The NiCoFe-LTH catalyst exhibited outstanding electrocatalytic activity with a low overpotential of 180 mV at an HER current density of 10 mA cm^{-2}, which is much lower than that of NiCo-LDH (200 mV) and bare Ni foam (340 mV) in 1 M KOH with 0.33 M urea (Fig. 4f) (note that the HER performance in 1 M KOH is almost the same with and without urea). The HER activity of NiCoFe-LTH/NF outperformed that of some previously reported transition metal-based composites in terms of overpotential (Table S2†). The Tafel slopes of all samples are shown in Fig. 4g. Pt exhibits the smallest Tafel slope of 65 mV dec^{-1}. The Tafel slope of NiCoFe-LTH is 78 mV dec^{-1}, which is much smaller than that of NiCo-LDH (95 mV dec^{-1}) and bare Ni foam (163 mV dec^{-1}). Fig. 4h shows the chronopotentiometric curve of NiCoFe-LTH/NF which displays excellent HER durability over 30 h at a current density of 10 mA cm^{-2}. The polarization curves before and after the long-term durability test (30 h) showed negligible changes, suggesting good durability of the catalyst (inset of Fig. 4h).

3.3 Origin of the enhanced catalytic activity

Generally, a larger surface area provides a higher number of active sites, which enhances the electrochemical performance.[68] Therefore, we first estimated the ECSA by calculating the double-layer capacitance (C_{dl}) from the CV curves measured at different scan rates (Fig. S3†). As shown in Fig. 5a, the NiCoFe-LTH/NF electrode has a larger C_{dl} value (22.33 mF cm^{-2}) than the NiCo-LDH/NF electrode (6.13 mF cm^{-2}). C_{dl} values are directly proportional to the ECSA, indicating that the NiCoFe-LTH/NF electrode exhibited a much larger ECSA than the NiCo-LDH/NF electrode, suggesting a greater number of active sites. Electrolyte resistance is associated with conductivity, which mainly affects the electrochemical performance.[69] Therefore, EIS was performed to further study the reaction kinetics of the electrode. The Nyquist plots in Fig. 5b suggest that NiCoFe-LTH/NF has a smaller charge transfer resistance (0.218 Ω) than pristine NiCo-LDH/NF (1.126 Ω). This indicates that the insertion of Fe facilitates the electrical conductivity of the NiCo-LDH/NF electrode owing to its large electrochemical surface area. The polarization resistances of NiCoFe-LTH/NF and NiCo-LDH/NF, which were estimated using electrochemical machining characteristic (ECM) fittings, are shown in Fig. 5c. To check the intrinsic activity of the catalyst, the TOF values were calculated using backward CV. The backward sweep of NiCoFe-LTH/NF and NiCo-LDH/NF was recorded at 200 mV s^{-1} in a 1 M KOH solution containing 0.33 M urea to calculate the exact number of electrochemically accessible sites for urea oxidation (Fig. 5d).

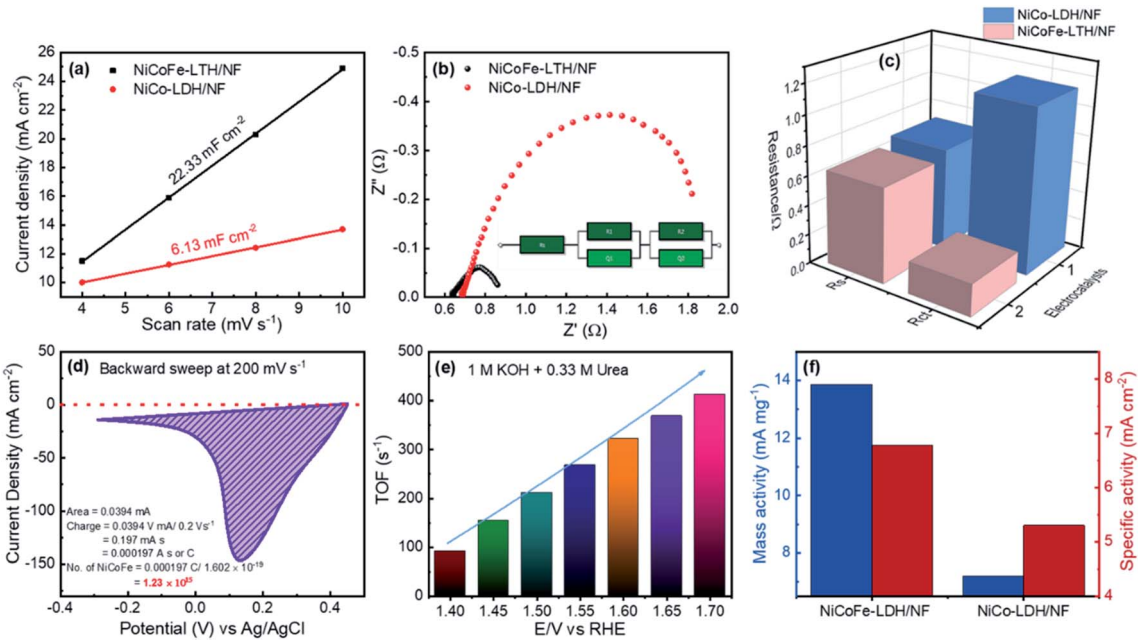

Fig. 5 (a) Capacitive current density *vs.* scan rate, (b) Nyquist plots of the NiCoFe-LTH/NF and NiCo-LDH/NF (inset: equivalent circuit), (c) corresponding polarization resistances obtained by ECM fitting of both electrodes, (d) backward CV of NiCoFe-LTH/NF for charge integration and calculation of electrochemically accessible sites, (e) plot of TOF against overpotential for the UOR (0.33 M urea in 1 M KOH) for NiCoFe-LTH/NF, (f) mass and specific activities of the electrocatalyst at the potential of 1.5 V (*vs.* RHE).

It was found that NiCoFe-LTH/NF had 1.23×10^{15} electrochemically accessible sites for urea oxidation. The corresponding TOFs, at various potentials, were calculated from eqn (1), using this value, as shown in Fig. 5e. The TOF value for urea oxidation increased with increasing potential, and the highest TOF value was observed at the vertex potential (1.70 V *vs.* RHE). The TOF values of NiCo-LDH/NF were similarly calculated (Fig. S4a†). At 1.70 V, NiCoFe-LTH shows a higher TOF value (412.70 s^{-1}) than NiCo-LDH/NF (346.14 s^{-1}) suggesting high intrinsic activity. In addition, the plot of TOF *versus* potential, for the UOR is displayed in Fig. S4b.† Fig. 5f shows the mass activity (MA) and specific activity (SA) values of NiCoFe-LTH/NF and NiCo-LDH/NF. At a potential of 1.5 V (*vs.* RHE) the MAs of NiCoFe-LTH/NF and NiCo-LDH/NF are 13.86 and 7.19 mA mg^{-1}, respectively. The SA values normalized by the BET surface area are 6.78 and 5.36 mA cm^{-2}, respectively, for NiCoFe-LTH/NF and NiCo-LDH/NF. The high MA and SA of NiCoFe-LTH/NF enhanced the electrochemical performance.

3.4 Electrochemical performances of a two-electrode system by integrating the UOR with the HER

The remarkable performance of NiCoFe-LTH/NF observed for both the UOR and HER suggests that NiCoFe-LTH/NF can be used for urea-electrolysis. Thus, NiCoFe-LTH/NF was utilized as both the anode and cathode to assemble the urea electrolyzer (Fig. 6a). Fig. 6b demonstrates that the full urea-electrolysis system offers greater thermodynamic and kinetic advantages in 1 M KOH with 0.33 M urea than pure water-splitting in the absence of urea. To deliver a current density of 10 mA cm^{-2}, a much larger voltage (1.65 V) is needed for the couple integrated with the HER and OER in the alkaline electrolyte. Upon the addition of urea, the voltage significantly reduced to 1.49 V at the same current density of 10 mA cm^{-2}. Gas bubbles generated at the electrode sides clearly implied greater hydrogen evolution and better energy conversion efficiency of urea-electrolysis. To reach current densities of 10, 20, 50, and 100 mA cm^{-2}, urea-electrolysis needs cell voltages of 1.49, 1.55, 1.67, and 1.81 V, respectively, whereas water-electrolysis needs much higher values of 1.65, 1.71, 1.81, and 1.94 V (Fig. 6c), clearly showing the superior cell efficiency of the urea electrolyzer. Stability is an important factor in practical applications in addition to a high catalytic performance. Chronoamperometric testing showed that the cell was able to deliver a current density of 10 mA cm^{-2}, while the final potential reached 1.52 V after 30 h of continuous operation (Fig. 6d and inset). These results indicate that the UOR was remarkably easier than the OER catalyzed by NiCoFe-LTH/NF at the anode. The electrode materials may undergo considerable changes under the high applied potentials of the OER and HER owing to the vigorous gas evolution. The quantity of H_2 evolved during urea-electrolysis from NiCoFe-LTH/NF was determined quantitatively by gas chromatography (Fig. 7). The amount of H_2 that was experimentally measured and theoretically calculated from the transferred charge showed nearly 92% faradaic efficiency for urea-electrolysis using NiCoFe-LTH/NF electrodes.

The remarkable electrocatalytic activity and stability of the NiCoFe-LTH/NF electrode can be ascribed to the following factors. (1) Fe incorporation alters the electronic structure and further promotes water dissociation and adsorption capacity.

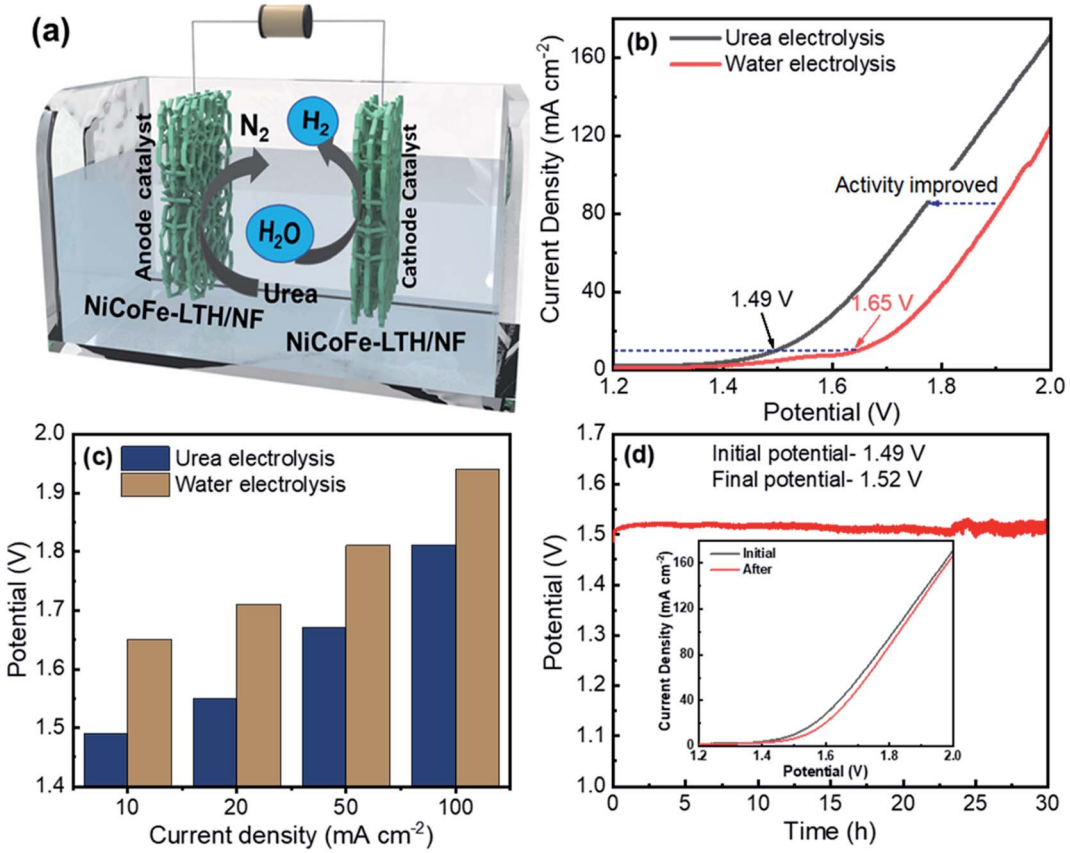

Fig. 6 (a) Schematic diagram of the urea electrolyzer using NiCoFe-LTH/NF as the anode and cathode, (b) comparative polarization curves for urea-electrolysis and water-electrolysis, (c) comparison of the cell voltage required to reach different current densities for urea-electrolysis and water-electrolysis, (d) long-term stability test of urea-electrolysis performed at a current density of 10 mA^{-2}, inset: the LSV curve of NiCoFe-LTH/NF before and after the stability test.

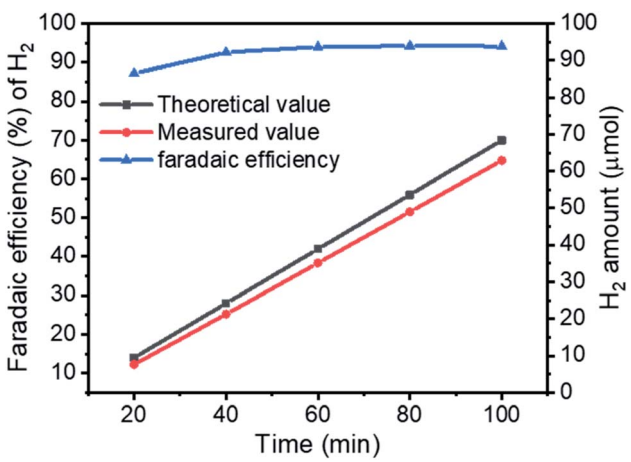

Fig. 7 Amount of H_2 theoretically calculated and experimentally measured and faradaic efficiency *versus* time for NiCoFe-LTH/NF during urea electrolysis.

(2) LTHs (brucite layers) with mixed valences of M^{2+} and M^{3+} (M = Ni/Co/Fe) have high intrinsic and catalytic activities for the UOR and HER. (3) The vertically aligned 2D-nanosheet structure of NiCoFe-LTH/NF provides a widely explored catalytic surface and excellent electron transport. (4) The excellent electrocatalytic stability may be achieved by the direct growth of NiCoFe-LTH/NF onto the NF substrate without the use of polymer binders, which offers good electrical connection and mechanical adhesion. (5) The highly open 2D nanosheet structure facilitates the release of gaseous products generated during the UOR and HER.

3.5 Physical characterizations of the NiCoFe-LTH electrode after the stability test

The electrochemical results show that the UOR, HER, and urea-electrolysis performance showed negligible changes after the stability tests. Herein, we also studied the morphology and composition of the catalyst after the long-term stability test. We employed FE-SEM and XPS to determine the changes in the electrodes after all the electrochemical studies. After the long-term chronopotentiometric stability tests for the UOR and HER, the nanosheet morphology of NiCoFe-LTH did not change significantly (Fig. S5a and b†). Fig. S6 and S7 in the ESI† show the XPS profiles of NiCoFe-LTH electrode materials after the stability tests for the UOR and HER, respectively. The XPS profiles of Ni, Co, Fe, and O are similar to the original spectra. Thus, NiCoFe-LTH/NF exhibits high electrochemical stability.

4. Conclusion

We have developed a NiCoFe-LTH/NF hybrid film prepared by a one-step hydrothermal method. The film acts as a high-performance cathode and anode electrocatalyst for urea-electrolysis to generate hydrogen and purify wastewater-containing urea. The Fe incorporation promotes a synergistic interplay between the three metals in NiCoFe-LTH and promotes the formation of oxyhydroxide species, which are proven to be the active species for the UOR and OER. Therefore, the as-deposited NiCoFe-LTH/NF exhibited outstanding catalytic activity, with a potential of 1.538 V to drive a current density of 25 mA cm^{-2} for the OER, and 1.379 V at 10 mA cm^{-2} for the UOR. Furthermore, electrolysis cells, constructed with NiCoFe-LTH/NF as the cathode and anode, exhibited interesting catalytic properties. These include achieving a current density of 10 mA cm^{-2} for water-splitting and urea-electrolysis at a cell voltage of 1.58 V and 1.49 V, respectively. This work could pave the way for the rational design of high-performance and cost-efficient electrocatalysts for urea-containing wastewater electrolysis from the viewpoint of practical applications.

Conflicts of interest

There are no conflicts to declare.

Acknowledgements

This work was supported by the Human Resources Development Program (No. 20194030202470) of the Korea Institute of Energy Technology Evaluation and Planning (KETEP) Grant funded by the Korean Government Ministry of Trade, Industry and Energy. This work was supported by the Technology Development Program to Solve Climate Changes of the National Research Foundation (grant no. 2016M1A2A2936784) funded by the Ministry of Science and ICT.

References

1 M. Cabán-Acevedo, M. L. Stone, J. R. Schmidt, J. G. Thomas, Q. Ding, H. C. Chang, M. L. Tsai, H. He and S. Jin, *Nat. Mater.*, 2015, **14**, 1245–1251.
2 K. Zeng, X. Zheng, C. Li, J. Yan, J. Tian, C. Jin, P. Strasser and R. Yang, *Adv. Funct. Mater.*, 2020, **30**, 2000503.
3 M. G. Schultz, T. Diehl, G. P. Brasseur and W. Zittel, *Science*, 2003, **302**, 624–627.
4 X. Sun and R. Ding, *Catal. Sci. Technol.*, 2020, **10**, 1567–1581.
5 G. Wang, Y. Ling, X. Lu, H. Wang, F. Qian, Y. Tong and Y. Li, *Energy Environ. Sci.*, 2012, **5**, 8215–8219.
6 B. K. Boggs, R. L. King and G. G. Botte, *Chem. Commun.*, 2009, **8**, 4859–4861.
7 X. Zhu, X. Dou, J. Dai, X. An, Y. Guo, L. Zhang, S. Tao, J. Zhao, W. Chu, X. C. Zeng, C. Wu and Y. Xie, *Angew. Chem., Int. Ed.*, 2016, **55**, 12465–12469.
8 N. Senthilkumar, G. Gnana kumar and A. Manthiram, *Adv. Energy Mater.*, 2018, **8**, 1702207.
9 R. Lan, S. Tao and J. T. S. Irvine, *Energy Environ. Sci.*, 2010, **3**, 438–441.
10 W. Xu, H. Zhang, G. Li and Z. Wu, *Sci. Rep.*, 2014, **4**, 1–6.
11 Z. Y. Yu, C. C. Lang, M. R. Gao, Y. Chen, Q. Q. Fu, Y. Duan and S. H. Yu, *Energy Environ. Sci.*, 2018, **11**, 1890–1897.
12 Y. Liang, Q. Liu, A. M. Asiri and X. Sun, *Electrochim. Acta*, 2015, **153**, 456–460.
13 L. Yan, Y. Sun, E. Hu, J. Ning, Y. Zhong, Z. Zhang and Y. Hu, *J. Colloid Interface Sci.*, 2019, **541**, 279–286.
14 L. Wang, S. Zhu, N. Marinkovic, S. Kattel, M. Shao, B. Yang and J. G. Chen, *Appl. Catal., B*, 2018, **232**, 365–370.
15 C. Li, Y. Liu, Z. Zhuo, H. Ju, D. Li, Y. Guo, X. Wu, H. Li and T. Zhai, *Adv. Energy Mater.*, 2018, **8**, 1801775.
16 Y. Tong, P. Chen, M. Zhang, T. Zhou, L. Zhang, W. Chu, C. Wu and Y. Xie, *ACS Catal.*, 2018, **8**, 1–7.
17 R. P. Forslund, C. T. Alexander, A. M. Abakumov, K. P. Johnston and K. J. Stevenson, *ACS Catal.*, 2019, **9**, 2664–2673.
18 G. Ma, Q. Xue, J. Zhu, X. Zhang, X. Wang, H. Yao, G. Zhou and Y. Chen, *Appl. Catal., B*, 2020, **265**, 118567.
19 D. Wang, W. Yan, S. H. Vijapur and G. G. Botte, *J. Power Sources*, 2012, **217**, 498–502.
20 D. Liu, T. Liu, L. Zhang, F. Qu, G. Du, A. M. Asiri and X. Sun, *J. Mater. Chem. A*, 2017, **5**, 3208–3213.
21 P. Babar, K. Patil, D. M. Lee, V. Karade, K. Gour, S. Pawar and J. H. Kim, *J. Colloid Interface Sci.*, 2021, **584**, 760–769.
22 L. Sha, J. Yin, K. Ye, G. Wang, K. Zhu, K. Cheng, J. Yan, G. Wang and D. Cao, *J. Mater. Chem. A*, 2019, **7**, 9078–9085.
23 P. Babar, A. Lokhande, V. Karade, I. J. Lee, D. Lee, S. Pawar and J. H. Kim, *J. Colloid Interface Sci.*, 2019, **557**, 10–17.
24 M. Song, Z. Zhang, Q. Li, W. Jin, Z. Wu, G. Fu and X. Liu, *J. Mater. Chem. A*, 2019, **7**, 3697–3703.
25 C. Xiao, S. Li, X. Zhang and D. R. MacFarlane, *J. Mater. Chem. A*, 2017, **5**, 7825–7832.
26 Y. Sun, S. Gao, F. Lei and Y. Xie, *Chem. Soc. Rev.*, 2015, **44**, 623–636.
27 M. S. Wu, G. W. Lin and R. S. Yang, *J. Power Sources*, 2014, **272**, 711–718.
28 R. Yang, Y. Zhou, Y. Xing, D. Li, D. Jiang, M. Chen, W. Shi and S. Yuan, *Appl. Catal., B*, 2019, **253**, 131–139.
29 Z. Yue, S. Yao, Y. Li, W. Zhu, W. Zhang, R. Wang, J. Wang, L. Huang, D. Zhao and J. Wang, *Electrochim. Acta*, 2018, **268**, 211–217.
30 P. Babar, A. Lokhande, V. Karade, B. Pawar, M. G. Gang, S. Pawar and J. H. Kim, *ACS Sustainable Chem. Eng.*, 2019, **7**, 10035–10043.
31 S. M. Pawar, B. S. Pawar, P. T. Babar, A. T. A. Ahmed, H. S. Chavan, Y. Jo, S. Cho, J. Kim, B. Hou, A. I. Inamdar, S. N. Cha, J. H. Kim, T. G. Kim, H. Kim and H. Im, *Appl. Surf. Sci.*, 2019, **470**, 360–367.
32 F. Lei, Y. Sun, K. Liu, S. Gao, L. Liang, B. Pan and Y. Xie, *J. Am. Chem. Soc.*, 2014, **136**, 6826–6829.
33 J. Xie, J. Zhang, S. Li, F. Grote, X. Zhang, H. Zhang, R. Wang, Y. Lei, B. Pan and Y. Xie, *J. Am. Chem. Soc.*, 2013, **135**, 17881–17888.

34 P. T. Babar, A. C. Lokhande, M. G. Gang, B. S. Pawar, S. M. Pawar and J. H. Kim, *J. Ind. Eng. Chem.*, 2018, **60**, 493–497.

35 Y. Sun, S. Wang, J. Ning, Z. Zhang, Y. Zhong and Y. Hu, *Nanoscale*, 2020, **12**, 991–1001.

36 T. Liu, D. Liu, F. Qu, D. Wang, L. Zhang, R. Ge, S. Hao, Y. Ma, G. Du, A. M. Asiri, L. Chen and X. Sun, *Adv. Energy Mater.*, 2017, **7**, 1700020.

37 S. Chen, J. Duan, A. Vasileff and S. Z. Qiao, *Angew. Chem., Int. Ed.*, 2016, **55**, 3804–3808.

38 Q. Liu, L. Xie, F. Qu, Z. Liu, G. Du, A. M. Asiri and X. Sun, *Inorg. Chem. Front.*, 2017, **4**, 1120–1124.

39 W. Zhu, M. Ren, N. Hu, W. Zhang, Z. Luo, R. Wang, J. Weng, L. Huang, Y. Suo and J. Wang, *ACS Sustainable Chem. Eng.*, 2018, **6**, 5011–5020.

40 R. Ding, L. Qi, M. Jia and H. Wang, *Nanoscale*, 2014, **6**, 1369–1376.

41 D. Wang, S. H. Vijapur, Y. Wang and G. G. Botte, *Int. J. Hydrogen Energy*, 2017, **42**, 3987–3993.

42 W. Yan, D. Wang and G. G. Botte, *J. Appl. Electrochem.*, 2015, **45**, 1217–1222.

43 Y. Song, J. Cheng, J. Liu, Q. Ye, X. Gao, J. Lu and Y. Cheng, *Appl. Catal., B*, 2021, **298**, 120488.

44 L. Hu, M. Li, X. Wei, H. Wang, Y. Wu, J. Wen, W. Gu and C. Zhu, *Chem. Eng. J.*, 2020, **398**, 125605.

45 X. Wang, Y. Tuo, Y. Zhou, D. Wang, S. Wang and J. Zhang, *Chem. Eng. J.*, 2021, **403**, 126297.

46 J. Chen, F. Zheng, S. J. Zhang, A. Fisher, Y. Zhou, Z. Wang, Y. Li, B. Bin Xu, J. T. Li and S. G. Sun, *ACS Catal.*, 2018, **8**, 11342–11351.

47 W. Zhu, R. Zhang, F. Qu, A. M. Asiri and X. Sun, *ChemCatChem*, 2017, **9**, 1721–1743.

48 L. Sha, K. Ye, G. Wang, J. Shao, K. Zhu, K. Cheng, J. Yan, G. Wang and D. Cao, *Chem. Eng. J.*, 2019, **359**, 1652–1658.

49 C. Huang, Y. Zhong, J. Chen, J. Li, W. Zhang, J. Zhou, Y. Zhang, L. Yu and Y. Yu, *Chem. Eng. J.*, 2021, **403**, 126304.

50 R. Fan, Q. Mu, Z. Wei, Y. Peng and M. Shen, DOI: 10.1039/d0ta03272g.

51 C. Li, X. J. Li, Z. Y. Zhao, F. L. Li, J. Y. Xue, Z. Niu, H. W. Gu, P. Braunstein and J. P. Lang, *Nanoscale*, 2020, **12**, 14004–14010.

52 Y. Jiao, C. Yang, H. Wang, Y. Zhong and Y. Hu, *J. Alloys Compd.*, 2022, **890**, 161929.

53 G. Rajeshkhanna, T. I. Singh, N. H. Kim and J. H. Lee, *ACS Appl. Mater. Interfaces*, 2018, **10**, 42453–42468.

54 Q. Yao, X. Zhou, S. Xiao, J. Chen, I. A. Abdelhafeez, Z. Yu, H. Chu and Y. Zhang, *Water Res.*, 2019, **165**, 114930.

55 N. L. W. Septiani, Y. V. Kaneti, Y. Guo, B. Yuliarto, X. Jiang, Y. Ide, N. Nugraha, H. K. Dipojono, A. Yu, Y. Sugahara, D. Golberg and Y. Yamauchi, *ChemSusChem*, 2020, **13**, 1645–1655.

56 C. Dong, X. Yuan, X. Wang, X. Liu, W. Dong, R. Wang, Y. Duan and F. Huang, *J. Mater. Chem. A*, 2016, **4**, 11292–11298.

57 S. Si, H. S. Hu, R. J. Liu, Z. X. Xu, C. Bin Wang and Y. Y. Feng, *Int. J. Hydrogen Energy*, 2020, **45**, 9368–9379.

58 D. Zha, H. Sun, Y. Fu, X. Ouyang and X. Wang, *Electrochim. Acta*, 2017, **236**, 18–27.

59 P. Ma, S. Luo, Y. Luo, X. Huang, M. Yang, Z. Zhao, F. Yuan, M. Chen and J. Ma, *J. Colloid Interface Sci.*, 2020, **574**, 241–250.

60 K. Patil, P. Babar, D. M. Lee, V. Karade, E. Jo, S. Korade and J. H. Kim, *Sustainable Energy Fuels*, 2020, **4**, 5254–5263.

61 X. L. Wang, L. Z. Dong, M. Qiao, Y. J. Tang, J. Liu, Y. Li, S. L. Li, J. X. Su and Y. Q. Lan, *Angew. Chem., Int. Ed.*, 2018, **57**, 9660–9664.

62 S. S. Wang, L. Jiao, Y. Qian, W. C. Hu, G. Y. Xu, C. Wang and H. L. Jiang, *Angew. Chem., Int. Ed.*, 2019, **58**, 10713–10717.

63 X. Yang, C. J. Wang, C. C. Hou, W. F. Fu and Y. Chen, *ACS Sustainable Chem. Eng.*, 2018, **6**, 2893–2897.

64 M. Gong, Y. Li, H. Wang, Y. Liang, J. Z. Wu, J. Zhou, J. Wang, T. Regier, F. Wei and H. Dai, *J. Am. Chem. Soc.*, 2013, **135**, 8452–8455.

65 M. Cheng, H. Fan, Y. Song, Y. Cui and R. Wang, *Dalton Trans.*, 2017, **46**, 9201–9209.

66 G. Liu, C. Shuai, Z. Mo, R. Guo, N. Liu, X. Niu, Q. Dong, J. Wang, Q. Gao, Y. Chen and W. Liu, *New J. Chem.*, 2020, **44**, 17313–17322.

67 C. Hu, L. Zhang, Z. J. Zhao, A. Li, X. Chang and J. Gong, *Adv. Mater.*, 2018, **30**, 1705538.

68 P. Babar, K. Patil, V. Karade, K. Gour, A. Lokhande, S. Pawar and J. H. Kim, *ACS Appl. Mater. Interfaces*.

69 A. N. Singh, M. H. Kim, A. Meena, T. U. Wi, H. W. Lee and K. S. Kim, *Small*, 2021, **17**, 2005605.